AIAA JOURNAL
Vol. 55, No. 1, January 2017

Multidimensional High-Resolution Schemes for Viscous Hypersonic Flows

Bernard Parent*
Pusan National University, Busan 46241, Republic of Korea

DOI: 10.2514/1.J055190

The first-order multidimensional flux difference splitting method (Parent, B., "Multidimensional Flux Difference Splitting Schemes," *AIAA Journal*, Vol. 53, No. 7, 2015, pp. 1936–1948) is here extended to second-order accuracy through the use of limiters. The proposed second-order flux functions are such that they collapse to the first-order multidimensional flux difference splitting stencil in the vicinity of discontinuities and tend toward second-order finite difference stencils in smooth parts of the solution. Various test cases of interest to hypersonic flight including supersonic ramp injectors, shock-induced boundary-layer separation, and hypersonic viscous layers reveal that the proposed method achieves as much as a four times increase in resolution per dimension over its first-order counterpart or over the second-order symmetric total variation diminishing schemes. When integrated through a block-implicit approach, this entails as much as a 40-fold increase in computational efficiency while not compromising the symmetric total variation diminishing reliable convergence to steady-state, essentially monotone solution, and high resolution of boundary layers.

Downloaded by PUSAN NATL. UNIV. on January 17, 2017 | http://arc.aiaa.org | DOI: 10.2514/1.J055190

Nomenclature

A, B, C	=	Jacobians of $\boldsymbol{F}$, $\boldsymbol{G}$, and $\boldsymbol{H}$ with respect to $\boldsymbol{U}$
a	=	speed of sound
a, b, c	=	wave speed along x, y, and z
D	=	Jacobian of $\boldsymbol{U}$ with respect to $\boldsymbol{Q}$
d	=	number of dimensions
E	=	$e + 0.5 \cdot \boldsymbol{v}^2$, total specific energy
e	=	specific energy
$\boldsymbol{F}, \boldsymbol{G}, \boldsymbol{H}$	=	convective flux vector along x, y, and z
f, g, h	=	convective flux along x, y, and z
I	=	identity matrix
i, j, k	=	grid indices
L	=	left eigenvector matrix
$\boldsymbol{M}$	=	vector of the limited characteristic variables
$\boldsymbol{N}$	=	vector of cross derivatives
$Pe_{\max}$	=	maximum cell Peclet number allowed when conditioning the eigenvalues
$Pe_{\Delta x}$	=	cell's Peclet number along x
$\boldsymbol{Q}$	=	vector of primitive variables
Re_{edge}	=	edge Reynolds number
s	=	characteristic length of a cell
t	=	time coordinate
$\boldsymbol{U}$	=	vector of conserved variables
u	=	conserved variable
$\boldsymbol{v}$	=	velocity vector
x, y, z	=	Cartesian coordinates
$\Delta x, \Delta y, \Delta z$	=	grid spacing along x, y, and z
$\delta_x(\cdot)$	=	discretization of $\partial_x(\cdot)$
$\partial_x(\cdot)$	=	partial derivative along x
ζ	=	entropy correction factor
ζ_d	=	entropy correction factor for Jacobians on denominator of the flux function
Θ	=	nondimensional matrix associated with the cross-difference terms
Λ	=	eigenvalue matrix
μ	=	viscosity
$\mu^\star$	=	effective viscosity including turbulence eddy viscosity
ρ	=	mass density
σ	=	spectral radius of flux Jacobian
Φ	=	limiter function matrix acting on the dissipative terms
Ψ	=	limiter function matrix acting on the cross-difference terms

Subscripts

r	=	rth row of vector
r, r	=	rth row and rth column of diagonal matrix

I. Introduction

HYPERSONIC viscous flows are a class of flowfields that are particularly challenging to simulate. Various difficulties arise in the hypersonic range that are nonexistent at lower speeds such as carbuncle phenomena, difficulty to capture shear stresses or heat fluxes within boundary layers, or loss of positivity or monotonicity in the vicinity of strong shocks.

A popular flux discretization strategy for hypersonic flow is the Roe flux difference splitting (FDS) scheme [1] turned second-order accurate through total variation diminishing (TVD) limiters applied to the characteristic variables [2] or to the primitive variables [3]. Such a discretization strategy is often preferred perhaps because of its following desirable attributes.

1) It yields essentially monotonic solutions, hence being capable to capture shock waves and other discontinuities with minimal spurious oscillations.

2) It can capture contact surfaces with minimal dissipation, hence being particularly well suited to solve viscous flows.

3) When noncompressive limiters are used, it exhibits good convergence characteristics, permitting the residual to be driven down to machine accuracy for a wide range of problems.

4) It is expressed in general matrix form, hence being straightforward to linearize or to extend to any system of conservation laws.

5) Its finite volume form permits fast convergence to steady state when used in conjunction with convergence acceleration techniques such as multigrid, block alternate-direction implicit (ADI), lower–upper symmetric Gauss–Seidel, etc.

The Roe flux difference splitting scheme turned second-order through TVD limiters is not without its flaws, however. One of its well-known drawbacks is its marked decrease of resolution when extended to multiple dimensions. Indeed, because the

Received 17 March 2016; revision received 18 June 2016; accepted for publication 5 August 2016; published online 24 October 2016. Copyright © 2016 by Bernard Parent. Published by the American Institute of Aeronautics and Astronautics, Inc., with permission. All requests for copying and permission to reprint should be submitted to CCC at www.copyright.com; employ the ISSN 0001-1452 (print) or 1533-385X (online) to initiate your request. Add last: See also AIAA Rights and Permissions www.aiaa.org/randp.

*Department of Aerospace Engineering; bernparent@gmail.com.

Downloaded by PUSAN NATL. UNIV. on January 17, 2017 | http://arc.aiaa.org | DOI: 10.2514/1.J055190

stencil was originally derived in one dimension, and because it is extended to multiple dimensions through dimensional splitting (by splitting the derivatives along each dimension and discretizing the so-obtained one-dimensional derivatives using one-dimensional operators), it is not genuinely multidimensional and hence leads to excessive dissipation of waves traveling obliquely to the grid lines.

To overcome the excessive dissipation of the dimensionally split stencil when simulating multidimensional problems, some remedies have been suggested. One such remedy is the rotation-interpolation approach, which consists of calculating the fluxes in a coordinate system that is rotated with respect to the grid instead of one aligned with the grid as in the dimensional splitting. Such a strategy has been shown to increase significantly the resolution when solving expansion fans and shock waves [4]. However, because the rotated frame of reference must be the same for all variables (the frame of reference is typically rotated following the flow velocity), not all waves can be captured with high resolution, and the use of the rotation-interpolation method can be a mixed blessing; whereas the resolution of expansion fans and shocks is enhanced, the resolution of shear waves is diminished [5]. Another attempt at extending the Roe approximate Riemann solver to multiple dimensions that has shown more promise is "residual distribution" as first proposed in [6]. The latter consists of distributing the flux integral at the cells interface (the residual) in a downwind manner, with the direction of downwinding being parallel to the waves and differing for each flux component. Although such has been demonstrated to yield a significantly superior resolution (especially for subsonic flows), it does also come with some disadvantages such as exhibiting convergence hangs or yielding a significantly lower resolution when simulating hypersonic flows [7].

Yet another genuinely multidimensional extension of FDS to multiple dimensions is through the use of the Cauchy–Kowalevski procedure. By modifying the Cauchy–Kowalevski procedure such that the time step that naturally appears within the flux function is replaced by a characteristic time step, some variants of FDS can be derived that are both genuinely multidimensional and in finite volume form. For instance, in [8], Huang and Lerat derive a multidimensional Roe scheme using the Cauchy–Kowalevski procedure that exhibits considerably higher resolution than the dimensionally split method for many problems of interest. However, the Huang–Lerat method introduces significant overshoots and undershoots of the properties in the vicinity of shock waves when the latter are not aligned with the mesh. Such was remedied in [9], where it was demonstrated that an essentially monotone solution can be obtained by splitting the cross-derivative terms among the several dimensions such that the coefficients of the cross derivatives remain small compared to the coefficients of the normal derivatives. Several test cases were then performed demonstrating a two-fold increase in resolution per dimension compared to the dimensionally split approach. The multidimensional flux difference splitting scheme developed in [9] was, however, first-order accurate.

In this paper, the multidimensional FDS [9] is extended to second-order accuracy such that the discretization stencil collapses to its first-order form in the vicinity of shocks or other discontinuities and becomes second-order accurate in smooth flow regions. Several test cases at high Mach number are then presented to determine the gains in resolution of the proposed multidimensional method to the commonly used dimensionally split second-order TVD schemes.

II. First-Order Multidimensional Flux Difference Splitting

As demonstrated in [9], a first-order-accurate multidimensional discretization of the wave equation

$$\frac{\partial u}{\partial t}+\frac{\partial f}{\partial x}+\frac{\partial g}{\partial y}+\frac{\partial h}{\partial z}=0 \tag{1}$$

can be derived using the Cauchy–Kowalevsky procedure by splitting the cross-derivative terms among the several dimensions such that the coefficients of the cross derivatives remains small compared to the coefficients of the normal derivatives. After some algebra, it was demonstrated that this would yield the following discretization equation:

$$\frac{u^{n+1}-u^n}{\Delta t}+\frac{f_{i+1/2}-f_{i-1/2}}{\Delta x}+\frac{g_{j+1/2}-g_{j-1/2}}{\Delta y}+\frac{h_{k+1/2}-h_{k-1/2}}{\Delta z}=0 \tag{2}$$

with the fluxes at the interfaces equal to

$$f_{i+1/2}=\frac{f_{i+1}+f_i}{2}-|a|_{i+1/2}\frac{u_{i+1}-u_i}{2}-\left(\frac{a\Delta y b\Delta x\delta_y u}{|a|\Delta y+|b|\Delta x}\right)_{i+1/2}-\left(\frac{a\Delta z c\Delta x\delta_z u}{|a|\Delta z+|c|\Delta x}\right)_{i+1/2} \tag{3}$$

$$g_{j+1/2}=\frac{g_{j+1}+g_j}{2}-|b|_{j+1/2}\frac{u_{j+1}-u_j}{2}-\left(\frac{a\Delta y b\Delta x\delta_x u}{|a|\Delta y+|b|\Delta x}\right)_{j+1/2}-\left(\frac{c\Delta y b\Delta z\delta_z u}{|c|\Delta y+|b|\Delta z}\right)_{j+1/2} \tag{4}$$

$$h_{k+1/2}=\frac{h_{k+1}+h_k}{2}-|c|_{k+1/2}\frac{u_{k+1}-u_k}{2}-\left(\frac{a\Delta z c\Delta x\delta_x u}{|a|\Delta z+|c|\Delta x}\right)_{k+1/2}-\left(\frac{c\Delta y b\Delta z\delta_y u}{|b|\Delta z+|c|\Delta y}\right)_{k+1/2} \tag{5}$$

and where $a\equiv\partial f/\partial u$, $b\equiv\partial g/\partial u$, $c\equiv\partial h/\partial u$, where the notation Δx refers to the grid spacing along x, whereas $\delta_x u$ refers to a discretization stencil approximating the partial derivative $\partial_x u$. Contrary to previous stencils derived from Cauchy–Kowalevski, the latter flux functions yield an "essentially monotone" solution (i.e., the solution may exhibit small spurious oscillations in the vicinity of discontinuities, but such overshoots or undershoots are quite small compared to the jump within the discontinuity.

We now wish to extend the latter to a system of conservation laws of the form:

$$\frac{\partial \boldsymbol{U}}{\partial t}+\frac{\partial \boldsymbol{F}}{\partial x}+\frac{\partial \boldsymbol{G}}{\partial y}+\frac{\partial \boldsymbol{H}}{\partial z}=0 \tag{6}$$

where $\boldsymbol{U}$ is the vector of conserved variables, and $\boldsymbol{F}$, $\boldsymbol{G}$, $\boldsymbol{H}$ are the convective flux vectors along x, y, z, respectively. We could extend the scalar flux functions outlined in Eqs. (3–5) to a system simply by replacing the scalar coefficients by their matrix analogues, as was done in [9]. Whereas such a strategy was shown successful in yielding monotone solutions for subsonic and supersonic flows, it was also found to yield near shock waves some overshoots and undershoots that were of importance when the Mach number was in the hypersonic range (i.e., when the Mach number is greater than 5 or so). Because such nonmonotonicity near discontinuities becomes amplified when the scheme is extended to second-order accuracy, it is here found necessary to remediate this problem.

To do so, first recall that the flux functions used herein are derived from a modified Cauchy–Kowalevski procedure, which is such that the coefficient of the cross-derivatives remains small compared to the one of the normal derivatives. Thus, small spurious oscillations introduced by the cross-derivatives are quickly damped by the dissipation originating from the normal derivatives. Although such a strategy is satisfactory for subsonic and supersonic flows, it is not as effective in the hypersonic range due to the temperature (and indirectly the pressure) being obtained from the internal energy, which itself is obtained from the difference between the total energy and the kinetic energy. In hypersonic flows for which most of the total

Downloaded by PUSAN NATL. UNIV. on January 17, 2017 | http://arc.aiaa.org | DOI: 10.2514/1.J055190

energy is kinetic, small amounts of nonmonotonicity on the total energy lead to orders-of-magnitude larger spurious oscillations on the temperature and pressure. Because such amplified oscillations associated with the cross-derivatives cannot be damped sufficiently rapidly by the dissipation introduced by the normal derivatives, significant overshoots and undershoots appear near shocks or other discontinuities.

A solution to this problem is to take the cross-derivatives of the primitive variables rather than to take the cross-derivatives of the conserved variables. Using primitive variables instead of the conserved variables is a strategy that is commonly used within the context of the monotone upwind schemes for scalar conservation laws (MUSCL) evolution-reconstruction procedure [3]. However, there is no evolution-reconstruction taking place in this case. Thus, we need to express the cross derivatives as a function of primitive variables by first noting that, if $\boldsymbol{U}$ can be expressed as a function of $\boldsymbol{Q}$, the following holds:

$$(\delta_y \boldsymbol{U})_{i+1/2} = D(\boldsymbol{U}_{i+1/2})\delta_y \boldsymbol{Q} \tag{7}$$

where $\boldsymbol{Q}$ is the vector of primitive variables, and where D is a square matrix composed of the derivatives of $\boldsymbol{U}$ with respect to $\boldsymbol{Q}$:

$$D(\boldsymbol{U}) \equiv \frac{\partial}{\partial \boldsymbol{Q}} \boldsymbol{U}(\boldsymbol{Q}) \tag{8}$$

To obtain essentially monotone solutions for hypersonic flows, it is important that the vector of primitive variables $\boldsymbol{Q}$ includes all independent determinative properties, with a determinative property being here defined as a property that must necessarily be positive for the system to be within physically valid bounds. For the perfect-gas Euler equations for which the vector of conserved variables is equal to $\boldsymbol{U} = [\rho, \rho \boldsymbol{v}_x, \rho \boldsymbol{v}_y, \rho \boldsymbol{v}_x, \rho E]^T$, we thus here set the primitive variables vector to $\boldsymbol{Q} = [\rho, \boldsymbol{v}_x, \boldsymbol{v}_y, \boldsymbol{v}_z, e]^T$. Then, the Jacobian D becomes

$$D = \begin{bmatrix} 1 & 0 & 0 & 0 & 0 \\ \boldsymbol{v}_x & \rho & 0 & 0 & 0 \\ \boldsymbol{v}_y & 0 & \rho & 0 & 0 \\ \boldsymbol{v}_z & 0 & 0 & \rho & 0 \\ E & \rho \boldsymbol{v}_x & \rho \boldsymbol{v}_y & \rho \boldsymbol{v}_z & \rho \end{bmatrix} \tag{9}$$

Thus, an essentially monotone first-order accurate flux difference splitting scheme can be obtained for a system of conservation laws starting from the scalar form outlined in Eqs. (3–5), substituting the scalar coefficients by their matrix counterparts, and modifying the discretization operators for the cross-derivatives as outlined in Eq. (7). This yields the following multidimensional FDS first-order flux functions:

$$\boldsymbol{F}_{i+1/2} = \frac{\boldsymbol{F}_{i+1} + \boldsymbol{F}_i}{2} - |A|_{i+1/2} \frac{\boldsymbol{U}_{i+1} - \boldsymbol{U}_i}{2} - (A\Delta y \Theta_{yx} D\delta_y \boldsymbol{Q})_{i+1/2} - (A\Delta z \Theta_{zx} D\delta_z \boldsymbol{Q})_{i+1/2} \tag{10}$$

$$\boldsymbol{G}_{j+1/2} = \frac{\boldsymbol{G}_{j+1} + \boldsymbol{G}_j}{2} - |B|_{j+1/2} \frac{\boldsymbol{U}_{j+1} - \boldsymbol{U}_j}{2} - (B\Delta x \Theta_{xy} D\delta_x \boldsymbol{Q})_{j+1/2} - (B\Delta z \Theta_{zy} D\delta_z \boldsymbol{Q})_{j+1/2} \tag{11}$$

$$\boldsymbol{H}_{k+1/2} = \frac{\boldsymbol{H}_{k+1} + \boldsymbol{H}_k}{2} - |C|_{k+1/2} \frac{\boldsymbol{U}_{k+1} - \boldsymbol{U}_k}{2} - (C\Delta x \Theta_{xz} D\delta_x \boldsymbol{Q})_{k+1/2} - (C\Delta y \Theta_{yz} D\delta_y \boldsymbol{Q})_{k+1/2} \tag{12}$$

where A, B, and C correspond to the convective flux Jacobians along x, y, and z, respectively (i.e., $A \equiv \partial \boldsymbol{F}/\partial \boldsymbol{U}$, $B \equiv \partial \boldsymbol{G}/\partial \boldsymbol{U}$, etc.), and where $|A|$, $|B|$, and $|C|$ stand for

$$|A| \equiv L^{-1}(A)|\Lambda(A)|L(A) \tag{13}$$

$$|B| \equiv L^{-1}(B)|\Lambda(B)|L(B) \tag{14}$$

$$|C| \equiv L^{-1}(C)|\Lambda(C)|L(C) \tag{15}$$

with $L(\cdot)$, $\Lambda(\cdot)$, and $L^{-1}(\cdot)$ the left eigenvector matrix, the eigenvalue matrix, and the right eigenvector matrix of the Jacobian $(\cdot)$, respectively. In [9], Θ_{xy} was set as

$$\Theta_{xy} \equiv (|A_x|\Delta y + |A_y|\Delta x)^{-1} A_x \Delta y \tag{16}$$

with $A_x \equiv \partial \boldsymbol{F}/\partial \boldsymbol{U}$, $A_y \equiv \partial \boldsymbol{G}/\partial \boldsymbol{U}$, etc. However, such involves a matrix inversion, which becomes expensive when the number of fluxes becomes large. At least for hypersonic flows, we find that such matrix inversion can be avoided while not compromising significantly on the resolution of the stencil by rather setting Θ_{xy} to

$$\Theta_{xy} \equiv \frac{\boldsymbol{v}_x \Delta y}{|\boldsymbol{v}_x|\Delta y + |\boldsymbol{v}_y|\Delta x} I \tag{17}$$

where $\boldsymbol{v}$ is the flow velocity vector, and I is the identity matrix. For all results shown in this paper, the latter formulation is chosen.

III. Extension to Second-Order Accuracy

We here seek second-order accurate extensions of the first-order multidimensional FDS scheme presented in the previous section that maintain the desirable properties of the first-order scheme. That is, the second-order stencils should be such that 1) they lead to essentially monotonic solutions even in the vicinity of strong shocks, 2) they do not induce convergence hangs for a wide range of flows from the subsonic to the hypersonic regime, 3) they can capture viscous layers with minimal dissipation, and 4) they are expressed in finite volume form.

To ensure that the converged solution is free of significant spurious oscillations, we will here follow a similar strategy as when extending the dimensionally split Roe scheme to second-order accuracy through TVD limiters. That is, the method should be such that it reverts to the first-order scheme in the vicinity of shock waves and becomes a second-order accurate stencil in smooth flow regions. Effectively, this entails that the terms added to the first-order FDS stencil needed to reach second-order accuracy should be limited such that they are progressively reduced as the property gradients increase.

Further, similar to the first-order flux functions outlined in the previous section, which collapse to the Roe scheme when there are no gradients in the second and third dimensions, it is desired that the multidimensional second-order flux functions proposed in this section collapse to the TVD schemes for one-dimensional problems.

We here avoid the use of compressive TVD limiters (such as Van Leer, superbee, van Albada, etc.) either deployed to all flux components or to only one component as in [10] because they often lead to convergence hangs. Although convergence stalls associated with compressive limiters can be prevented by not limiting entirely the second-order terms, such yields solutions tainted with significant spurious oscillations even in the transonic regime where the shock waves are weak [11]. Because both monotonicity of the solution and convergence without stall are here deemed important properties of the numerical method, we hence use exclusively noncompressive minmod limiters, which allow the residual to be converged down to machine accuracy for a wide range of problems.

Some flux functions that do satisfy the aforementioned requirements are the following:

$$\boldsymbol{F}_{i+1/2} = \frac{1}{2}(\boldsymbol{F}_{i+1} + \boldsymbol{F}_i) - \frac{1}{2}L^{-1}(A)_{i+1/2}|\Lambda(A)_{i+1/2}|\boldsymbol{M}(A)_{i+1/2} - \frac{1}{4}(A\Theta_{yx}\boldsymbol{N}_j + A\Theta_{zx}\boldsymbol{N}_k)_{i+1/2} \tag{18}$$

$$\boldsymbol{G}_{j+1/2} = \frac{1}{2}(\boldsymbol{G}_{j+1} + \boldsymbol{G}_j) - \frac{1}{2}L^{-1}(B)_{j+1/2}|\Lambda(B)_{j+1/2}|\boldsymbol{M}(B)_{j+1/2} - \frac{1}{4}(B\Theta_{xy}\boldsymbol{N}_i + B\Theta_{zy}\boldsymbol{N}_k)_{j+1/2} \tag{19}$$

$$\boldsymbol{H}_{k+1/2} = \frac{1}{2}(\boldsymbol{H}_{k+1} + \boldsymbol{H}_k) - \frac{1}{2}L^{-1}(C)_{k+1/2}|\Lambda(C)_{k+1/2}|\boldsymbol{M}(C)_{k+1/2} - \frac{1}{4}(C\Theta_{xz}\boldsymbol{N}_i + C\Theta_{yz}\boldsymbol{N}_j)_{k+1/2} \tag{20}$$

where $\boldsymbol{M}$ is a vector related to the limited characteristic variables:

$$\boldsymbol{M}(\cdot)_{i+1/2} = (I - \Phi(\cdot)_{i+1/2})L(\cdot)_{i+1/2}(\boldsymbol{U}_{i+1} - \boldsymbol{U}_i) \tag{21}$$

where I is the identity matrix, and Φ is a limiter function composed of diagonal elements of the form:

$$[\Phi(\cdot)_{i+1/2}]_{r,r} = \frac{\text{minmod}([L(\cdot)_{i-1/2}(\boldsymbol{U}_i - \boldsymbol{U}_{i-1})]_r, [L(\cdot)_{i+1/2}(\boldsymbol{U}_{i+1} - \boldsymbol{U}_i)]_r, [L(\cdot)_{i+3/2}(\boldsymbol{U}_{i+2} - \boldsymbol{U}_{i+1})]_r)}{[L(\cdot)_{i+1/2}(\boldsymbol{U}_{i+1} - \boldsymbol{U}_i)]_r} \tag{22}$$

where the minmod function returns the argument with the lowest magnitude if all its arguments share the same sign and zero otherwise.

In addition, the cross-derivative vector $\boldsymbol{N}_j$ is limited through a minmod such that it reverts to its first-order-accurate counterpart in regions of sharp gradients while vanishing in smooth regions:

$$(\boldsymbol{N}_j)_{i+1/2} = D_{i+1/2}(I - (\Psi_j)_{i+1/2})(\boldsymbol{Q}_{i,j+1} + \boldsymbol{Q}_{i+1,j+1} - \boldsymbol{Q}_{i,j-1} - \boldsymbol{Q}_{i+1,j-1}) \tag{23}$$

where Ψ_j is a limiter function diagonal matrix associated with the cross-derivative terms along j. To preserve monotonicity, it is important that Ψ (a function used to limit the cross-difference terms) approaches zero at a similar rate as Φ (a function used to limit the dissipative terms) does. Should Ψ and Φ not vary in close synchronization, spurious oscillations may form because the cross-derivative terms are antidissipative and can only be fully added to the normal difference terms when the latter become a first-order upwinded stencil (i.e., when Φ becomes 0). For this reason, we model the minmod operator within the cross-difference terms on the one within the dissipative terms as follows:

The latter limiter function will effectively lead to the cross difference terms and the dissipative terms being limited in close synchronization because both limiter functions Ψ and Φ share the following three attributes: 1) the term on the denominator of the limiter matches the spatial gradient within the flux function that is eventually multiplied by the limiter; 2) the minmod function is used to limit the gradients; and 3) when the gradients within the minmod function are uniform, the limiter function becomes 1.

It can be easily shown that, in regions of sharp gradients, the limiter matrices Φ and Ψ become zero, which leads to the second-order flux functions outlined in Eqs. (18–20) collapsing to the first-order multidimensional flux functions outlined in Eqs. (10–12). On the other hand, as the slope of the flow properties becomes constant through the stencil (as occurs in "smooth" flow regions as the mesh is refined), the limiter matrices Φ and Ψ become equal to the identity matrix, effectively transforming the flux functions [Eqs. (18–20)] into centered second-order accurate stencils.

In the absence of gradients along the second and third dimensions, the flux functions proposed previously can be demonstrated to collapse to the Yee symmetric total variation diminishing (STVD) scheme [2,12], which limits the slope of the characteristic variables while avoiding a reconstruction of states at the interface. This is in contrast to the Anderson–Thomas–Van Leer MUSCL reconstruction-evolution procedure [3], which limits the slope of the primitive variables needed to reconstruct the left and right states of the Roe Riemann solver at the interface. It is here preferred not to use a reconstruction evolution because such can lead to a low resolution of the skin friction and the surface heat flux associated with hypersonic boundary layers, as will be outlined in Sec. VI.

Although the proposed flux functions have significantly more terms than the STVD and are hence more expensive to compute, such does not translate into a significant increase in computing effort per iteration as long as a block-implicit integration strategy is used. As shown in Table 1 ([13–15]), the present method combined with a block ADI or diagonally dominant alternate-direction implicit (DDADI) requires between 2 and 22% more CPU time per iteration compared to the STVD, with the differences becoming smaller as the number of transport equations comprising the physical model increases.

IV. Eigenvalue Conditioning

Because the Euler equations accept entropy-decreasing phenomena to form, a carbuncle phenomenon can occur when

$$[(\Psi_j)_{i+1/2}]_{r,r} = \frac{4 \cdot \text{minmod}([\boldsymbol{Q}_{i,j+1} - \boldsymbol{Q}_{i,j}]_r, [\boldsymbol{Q}_{i,j} - \boldsymbol{Q}_{i,j-1}]_r, [\boldsymbol{Q}_{i+1,j+1} - \boldsymbol{Q}_{i+1,j}]_r, [\boldsymbol{Q}_{i+1,j} - \boldsymbol{Q}_{i+1,j-1}]_r)}{[\boldsymbol{Q}_{i,j+1} + \boldsymbol{Q}_{i+1,j+1} - \boldsymbol{Q}_{i,j-1} - \boldsymbol{Q}_{i+1,j-1}]_r} \tag{24}$$

Table 1 Ratio between the proposed scheme CPU time and the STVD CPU time

	Pseudotime integration		
Physical system	Explicit Euler	Block ADI	Block DDADI [13,14]
Navier–Stokes perfect gas	1.50	1.22	1.16
Favre–Reynolds real gas four-species[a]	1.18	1.09	1.06
Favre–Reynolds plasma eight-species[b]	1.06	1.03	1.02

[a]The "Favre–Reynolds real gas" physical model includes temperature-dependent specific heats, mass conservation equations for each species, the nitrogen vibrational energy transport equation, the turbulence kinetic energy transport equation, and the turbulence kinetic energy specific dissipation rate transport equation.

[b]The "Favre–Reynolds plasma" physical model consists of the Favre–Reynolds real gas transport equations (modified for plasma effects) along with an extra transport equation for the potential equation [15].

Downloaded by PUSAN NATL. UNIV. on January 17, 2017 | http://arc.aiaa.org | DOI: 10.2514/1.J055190

simulating blunt bodies at hypervelocities. This can be remedied in some cases by simply conditioning the acoustic waves (i.e., the eigenvalues that have the form $\boldsymbol{v}_x + a, \boldsymbol{v}_x - a$) within the eigenvalue matrices. Such is not sufficient to prevent a carbuncle in the general case, however, and it is necessary to also condition the convective waves to unconditionally prevent aphysical phenomena to form. Conditioning the convective waves does present a challenge because it leads to excessive dissipation within viscous layers effectively preventing the flux discretization scheme to capture the shear stress and the thickness of high-Reynolds-number boundary layers with a limited number of nodes. A remedy was proposed by Gnoffo and White in [16], where the conditioning is made a function of the edge Reynolds number, which is defined as

$$Re_{\text{edge}} \equiv \frac{\rho a s}{\mu} \tag{25}$$

where a is the speed of sound, and s is some reference length obtained from the volume and the area of the cells on the left and right of the interface (see [16] for more details). However, when used in conjunction with the STVD scheme or the proposed stencil, such is found to introduce nonnegligible dissipation near the leading-edge of flat plates where less than five gridlines or so are located within the boundary layer. This in turn taints the skin friction with some dissipation for a considerable distance downstream. We thus here find it necessary to improve the Gnoffo and White technique [16] by making the eigenvalue conditioning function of the cell Peclet number rather than the edge Reynolds number, so that the eigenvalue conditioning is switched off within boundary layers even when the latter are resolved with very few nodes. For all eigenvalues of the x-aligned fluxes (i.e., both the acoustic and convective waves of the convective flux Jacobian A), the conditioning proposed hence takes on the form:

$$[|\Lambda(A)|]_{r,r} \rightarrow [|\Lambda(A)|]_{r,r} + \zeta a \max\left(0, \frac{\Delta x}{\max(\Delta x, \Delta y, \Delta z)} - \frac{1}{\min(Pe_{\max}, Pe_{\Delta x})}\right) \tag{26}$$

where a is the sound speed, and $Pe_{\Delta x}$ is the cell's Peclet number along x:

$$Pe_{\Delta x} \equiv \frac{\rho |\boldsymbol{v}_x| \Delta x}{\mu^\star} \tag{27}$$

where $\boldsymbol{v}_x$ is the velocity in the x direction, $\mu^\star$ is the effective viscosity (including the turbulence eddy viscosity if a turbulence model is used), ρ is the density, and Δx is the grid spacing along x. Note that the Peclet number is here used in the context of momentum transfer and corresponds to the ratio of the rate of advection of momentum to the rate of diffusion of momentum. Although similar in form, the Peclet number for momentum transfer differs from the Reynolds number by including the effect of turbulence eddy momentum diffusion (i.e., it is a function of $\mu^\star$ and not simply of μ). Because the turbulence eddy viscosity can differ from the molecular viscosity by an order of magnitude or more within the boundary layer, it is important to use here the cell's Peclet number and not the cell's Reynolds number when limiting the entropy correction.

In Eq. (26), ζ is a user-specified constant typically set to 0.1. Because the conditioning proposed in Eq. (26) is a function of the cell's aspect ratio (through the term $\Delta x / \max(\Delta x, \Delta y, \Delta z)$), the amount of dissipation added along the dimension with the smallest spacing is less than the dissipation added along the dimension with the largest spacing. This reduces considerably the dissipation within high-speed boundary layers where the mesh is clustered near the surfaces because of the high aspect ratio of the cells in such flow regions. Further, should the ratio between the mesh spacing and the maximum mesh spacing be less than $1/Pe_{\max}$, no entropy correction is applied. Effectively, this turns off the entropy correction along the dimension with the smallest mesh spacing for cells that have an aspect ratio of more than $Pe_{\max}$, with the latter being a user-specified constant typically set to 20. Further, the minimum between $Pe_{\max}$ and the cell's Peclet number is taken to ensure that, should the physical dissipation be higher than the numerical dissipation, no entropy correction is applied because it is not needed.

The conditioning of the eigenvalues of the y- and z-aligned fluxes can be obtained similarly as in Eq. (26) by substituting the velocity component and the grid spacing along x by their counterparts along y and z, respectively.

As for the wave speeds appearing on the denominator of the flux function, they must also be conditioned to avoid a singularity. Because conditioning the wave speeds on the denominator of the flux functions does not lead to a loss of resolution of viscous layers, it can be performed in the standard manner as follows:

$$[|\Lambda(A)|]_{r,r} \rightarrow [|\Lambda(A)|]_{r,r} + \zeta_d \sigma \tag{28}$$

where σ is the spectral radius of the flux Jacobian, and ζ_d is a user-specified constant typically set to 0.1. Of course, should ζ_d be set to a large positive value approaching infinity, the cross-derivative terms would become negligible compared to the other terms, and the multidimensional flux function would hence revert to its dimensionally split counterpart. As will be shown in Sec. VI, the cross-derivative terms do increase the resolution significantly for many multidimensional problems of interest, and it is hence important to keep ζ_d to low values to obtain a high resolution.

V. Interface Averaging

How the properties are averaged at the interfaces between cells can have a significant impact on the resolution of flux difference splitting schemes. For instance, in [1], Roe demonstrates that, should the properties at the $i + 1/2$ interface be averaged such that the following holds:

$$\boldsymbol{F}_{i+1} - \boldsymbol{F}_i = A_{i+1/2}(\boldsymbol{U}_{i+1} - \boldsymbol{U}_i) \tag{29}$$

the flux function can capture a contact discontinuity within once cell. The averaging proposed by Roe yields gains in resolution not only for one-dimensional flows but also for multidimensional problems as long as the grid is aligned (or closely aligned) with the streamlines. For instance, when using the Roe averaging procedure on two-dimensional structured meshes, high-Reynolds-number boundary layers can be resolved with minimal dissipation because the grid is closely aligned with the streamlines near the surfaces. Because the multidimensional flux function proposed herein does revert to its dimensionally split counterpart when the grid is aligned with the waves, and because it is desired to capture high-Reynolds-number boundary layers with high resolution, we here follow [1] and apply the Roe averaging procedure when determining the eigenvalues and eigenvectors at the interface of cells. However, this is performed only for the eigenvalues and eigenvectors at the interfaces part of the normal derivative terms [the first two terms on the right-hand side of Eqs. (18–20)].

As for the cross-derivative terms, Roe averaging does not yield a higher resolution of viscous layers whether they are aligned with the mesh or not. Rather, the properties at the interface within the cross derivatives are here averaged such that they minimize spurious oscillations near discontinuities. This can be accomplished by averaging Θ at the interface from the minmod of the left and right states as follows:

$$[\Theta_{i+1/2}]_{r,r} = \text{minmod}([\Theta_i]_{r,r}, [\Theta_{i+1}]_{r,r}) \tag{30}$$

Such an averaging procedure helps in maintaining monotonicity near strong shocks and discontinuities, especially in the hypersonic regime. Indeed, it is recalled that the cross-difference terms have been derived such that the small spurious oscillations that they introduce in the vicinity of shocks or other discontinuities are damped by the dissipation introduced by the normal derivatives. For such a strategy to yield essentially monotonic solutions, it is important that the magnitude of the interface coefficients multiplying the cross

Downloaded by PUSAN NATL. UNIV. on January 17, 2017 | http://arc.aiaa.org | DOI: 10.2514/1.J055190

Downloaded by PUSAN NATL. UNIV. on January 17, 2017 | http://arc.aiaa.org | DOI: 10.2514/1.J055190

derivatives does not exceed too significantly the one of the interface coefficients multiplying the normal derivatives. In regions with high multidimensional gradients (such as in the vicinity of strong oblique shocks in the hypersonic regime for instance), this is satisfied by building the cross-derivative coefficients from the minmod of the primitive variables on the adjacent nodes as specified in Eq. (30).

VI. Test Cases

Let us now proceed to assess the gains in resolution of the proposed genuinely multidimensional flux functions over their dimensionally split counterparts. For all test cases, the eigenvalue conditioning parameters ζ and ζ_d are both set to 0.1. The system of equations considered is the perfect-gas Euler or Navier–Stokes equations in generalized coordinates with the specific heat ratio set to 1.4 and the gas constant set to 287 $\mathrm{J}/(\mathrm{kg}\cdot\mathrm{K})$. When solving viscous flows, the viscous terms are discretized using second-order centered stencils, with the thermal conductivity and the viscosity set to 0.03 $\mathrm{W}/(\mathrm{m}\cdot\mathrm{K})$ and $2\cdot10^{-5}$ $\mathrm{kg}/(\mathrm{m}\cdot\mathrm{s})$, respectively. Such a physical model is here chosen for its simplicity and to make the results more easily reproducible. Nonetheless, it has been verified that similar gains in resolution could be obtained for more accurate physical models including real gas effects and additional transport equations to account for a two-equation turbulence model, multiple species, and the nitrogen vibrational energy in nonequilibrium.

In rewriting the flux functions outlined in Eqs. (18–20) from Cartesian to generalized coordinates, the grid spacings Δx, Δy, and Δz are set to 1, whereas the vector of conserved variables, the convection flux vector, the convective flux Jacobians, the eigenvector matrices, and the eigenvalue matrices are set to their curvilinear counterparts. The eigenvectors of the Euler equations in multiple dimensions are not unique (there is an infinity of possible solutions), and how they are chosen does have an impact on the solution, although such is generally negligible. Nonetheless, to reproduce the results shown herein exactly, one should use the eigenvectors outlined in the appendix of [17].

Because several of the flows here considered involve a large disparity of time scales originating from the viscous effects, it is considered most efficient to converge the discretized equations through a block ADI method using local pseudotime relaxation. Such alleviates the stiffness associated with the viscous terms and permits large pseudotime steps to be used leading to fast convergence. The convergence to steady state is further accelerated through the use of the multizone acceleration technique outlined in [18].

In assessing the gains of resolution of the multidimensional flux functions, comparisons are here performed with standard dimensionally split flux functions based on the Roe FDS turned second-order accurate either through the Yee TVD limiters applied to the characteristic variables [2] or through the Anderson–Thomas–Van Leer MUSCL reconstruction-evolution procedure [3]. The MUSCL reconstruction is here obtained through an extrapolation of the density, temperature, and velocities. Although interpolating the effective pressure (including the contribution from the turbulence kinetic energy) instead of the temperature would result in a higher resolution of the viscous layers, such is possible only if the FDS solver is applied to all transport equations (including the turbulence kinetic energy equation) conjunctly, which is seldom the case.

A. Shear Wave

The first test case considered consists of a Mach 1.98 jet at a temperature of 300 K flowing parallel to a Mach 3.05 jet at a temperature of 600 K, with both jets having a pressure of 0.1 bar at the domain entrance. Because the viscosity and thermal conductivity are set to zero, the exact solution to this problem is trivial; both jets should remain undisturbed separated from each other by an infinitely thin shear wave.

When the grid is aligned with the shear wave, the Roe scheme can capture this problem exactly because the interface averaging is such that a contact discontinuity (or a shear wave) can be captured within one cell. However, when the grid is misaligned at an angle of 30 deg with respect to the shear wave (as is the case here), the dimensionally split methods introduce significant dissipation, and the shear wave spreads artificially as the flow progresses downstream. This is remedied to a significant degree through the use of a genuinely multidimensional scheme, which, through the Mach number contours in Fig. 1 using a 60^2 grid, can be seen to result in a significant reduction of the spreading of the contact discontinuity.

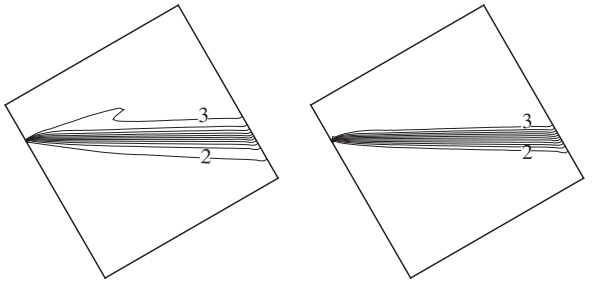

a) STVD b) Present

Fig. 1 Streamwise Mach number contours for the shear-wave case on an orthogonal mesh.

Interestingly, whether the mesh is orthogonal or significantly skewed does not affect too considerably the gains in resolution. For instance, consider the same shear wave test case as before but with the orthogonal mesh substituted by a skewed mesh (with half the cells corners having angles of 45 deg and the other half having angles of 135 deg). As attested by the Mach number contours in Fig. 2, the proposed method still offers a significant gain in resolution over the STVD when used on skewed cells. Therefore, should it be deployed to unstructured meshes with mixed elements (which share similar characteristics as structured meshes with skewed cells), the present scheme is hence expected to also offer significant gains in resolution over the STVD, albeit of less importance than reported here on a structured near-orthogonal mesh.

B. Wavy Wall

The second test case consists of a Mach 2 flow at a pressure of 0.1 bar and a temperature of 300 K entering a channel in which the bottom wall position is made proportional to a sine function. Because such a "wavy-wall" channel generates multiple oblique shocks, compression fans, and expansion fans that interact with each other creating complex wave patterns that are representative of flows found in supersonic inlets or scramjet combustors, it constitutes a particularly good test case to assess the performance gains of our multidimensional scheme for some problems of interest to supersonic flight.

A comparison of the pressure contours on various grid sizes in Fig. 3 shows that the proposed multidimensional scheme achieves close to a

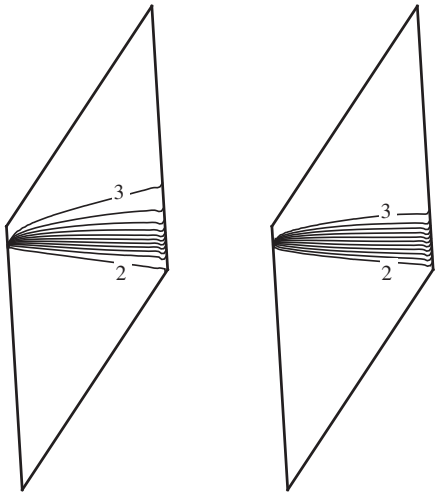

a) STVD b) Present

Fig. 2 Streamwise Mach number contours for the shear-wave case on a skewed mesh.

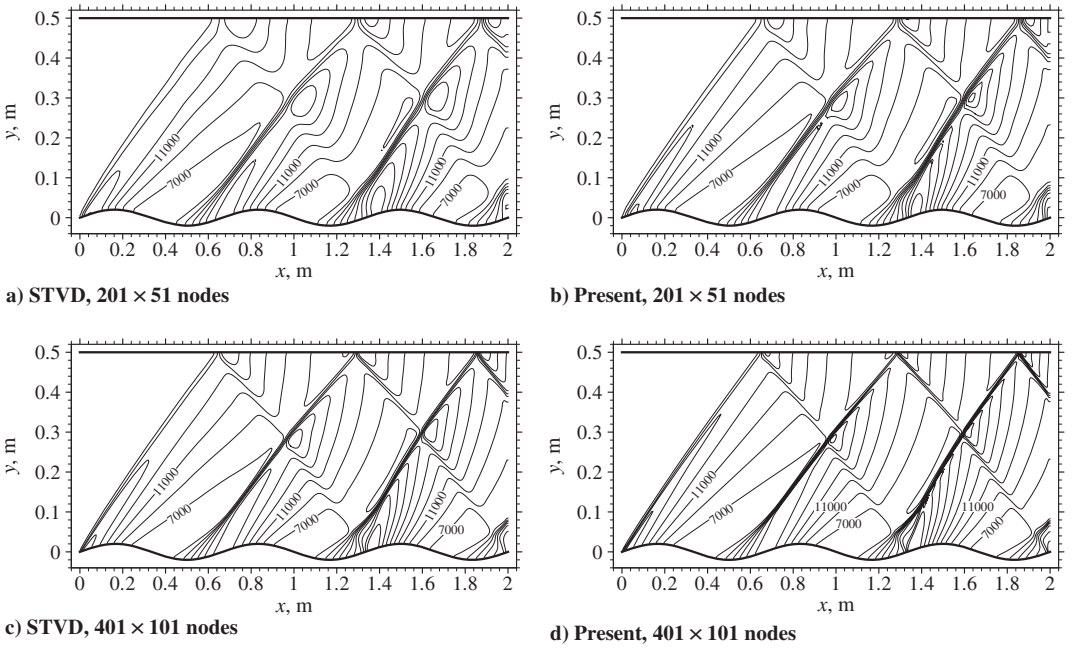

Fig. 3 Pressure contours (in pascals) for the Mach 2 wavy-wall case.

Downloaded by PUSAN NATL. UNIV. on January 17, 2017 | http://arc.aiaa.org | DOI: 10.2514/1.J055190

twofold increase in resolution per dimension compared to its dimensionally split counterpart. That is, for a desired level of resolution, the use of the proposed approach permits the mesh size to be reduced by almost four times for this two-dimensional problem. What makes this gain in resolution especially appealing is that it is obtained while not sacrificing the convergence capabilities of the STVD scheme. This is in contrast to alternative approaches, such as the Van Leer limiter or weighted essentially nonoscillatory (WENO), which achieve higher resolution at the expense of convergence hangs. Indeed, as can be seen from the residual histories in Fig. 4, the residual of the proposed multidimensional scheme converges down to machine accuracy, whereas the one of the MUSCL scheme with a Van Leer limiter hangs after less than one order of magnitude of convergence. Such good convergence behavior is not limited to this flowfield in particular; for all test cases outlined in this paper, it was verified that the proposed stencils did not result in convergence hangs.

C. Blunt Body

A third key problem that is often used to test numerical methods is supersonic flow over a blunt body. Such can be challenging to capture because it often leads to a carbuncle phenomenon (i.e., an aphysical wave that prevents the bow shock from stabilizing), which originates from the Euler equations allowing entropy-decreasing waves to form. Although this could be remedied simply by adding viscous terms and making sure that the mesh is fine enough to capture viscous effects occurring within the shock wave, this strategy would be cumbersome for typical bow shocks forming on flight vehicles because the shock-wave thickness in sea-level air is of the order of microns, and reducing the mesh spacing to micrometer scale would require excessive computing resources. Rather, to prevent a carbuncle from forming, it is more computationally efficient to add some numerical dissipation to the discretized equations to mimic the effect of the physical dissipation. This is here accomplished by conditioning the eigenvalues as outlined previously in Sec. IV.

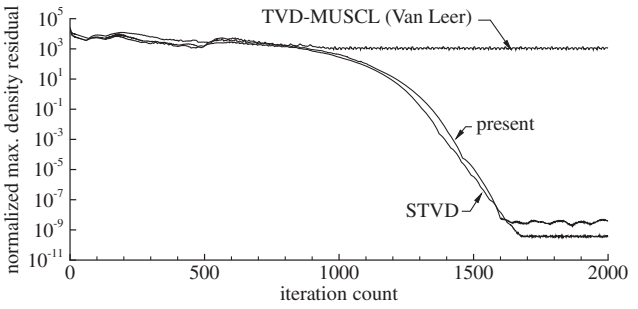

Fig. 4 Residual convergence history comparison for the wavy-wall test case at a Courant-Friedrich-Lewy number of 1.0 and a mesh of 401 × 101 nodes.

We here test our eigenvalue conditioning for a Mach 3 flow at a pressure of 10.2 kPa and a temperature of 300 K interacting with a blunt body in the shape of an ellipse. To make the problem more susceptible to a carbuncle, the computational domain surrounds the blunt body using the same mesh as depicted in [9]. Such problem setup and grid were found to create a carbuncle with the proposed method as well as with the STVD scheme should the convective and acoustic waves not be conditioned. However, a carbuncle could be avoided when conditioning the eigenvalues with ζ set to 0.1.

As attested by the pressure coefficient contours shown in Fig. 5, and in contrast to previous finite volume schemes derived from Cauchy–Kowalevski, the proposed method yields an essentially monotone solution in the vicinity of the bow shock whether or not the mesh is aligned with the wave. Further, because the present scheme includes cross-derivative terms, it exhibits a higher resolution than the STVD in the vicinity of the shock when the latter is misaligned with the mesh. Such high resolution is not limited to this Mach number in particular; throughout the freestream Mach number range 3–30, the proposed method has been verified to yield a solution that is free of spurious oscillations and that has a higher resolution than the STVD.

It may be argued that the proposed method is more likely to produce a carbuncle because it introduces less dissipation near the discontinuity. However, it has been verified that this is not the case and that the higher resolution near the bow shock is obtained without an associated drawback. For instance, consider the same blunt body geometry but with the incoming Mach number set to 8 to increase the likelihood of a carbuncle. As can be seen from the density contours in Fig. 6, the proposed method requires less, not more, additional dissipation to prevent a carbuncle. Thus, not only does the present scheme provide a higher resolution of the shock for a given entropy correction factor, but it is less susceptible to yield a carbuncle. In turn, this permits the use of lower values of the entropy correction, resulting in even higher resolution.

D. Hypersonic Boundary Layer

Flow features that can be challenging to capture with high resolution using compressible flow schemes are rarefaction fans

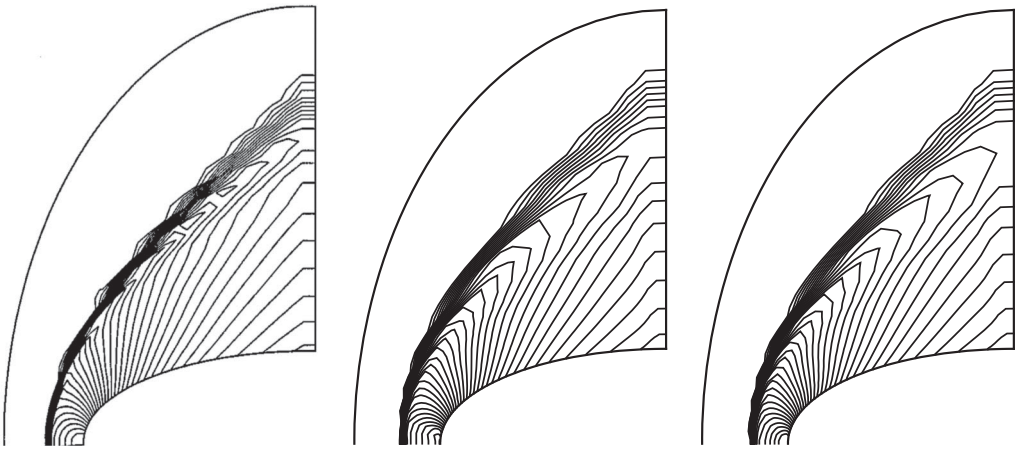

a) Huang-Lerat [8] b) Present c) STVD

Fig. 5 Pressure coefficient profiles for the blunt body case at Mach 3 using a 64×33 mesh. Figure 5a is reprinted from [8] with permission from Elsevier.

Downloaded by PUSAN NATL. UNIV. on January 17, 2017 | http://arc.aiaa.org | DOI: 10.2514/1.J055190

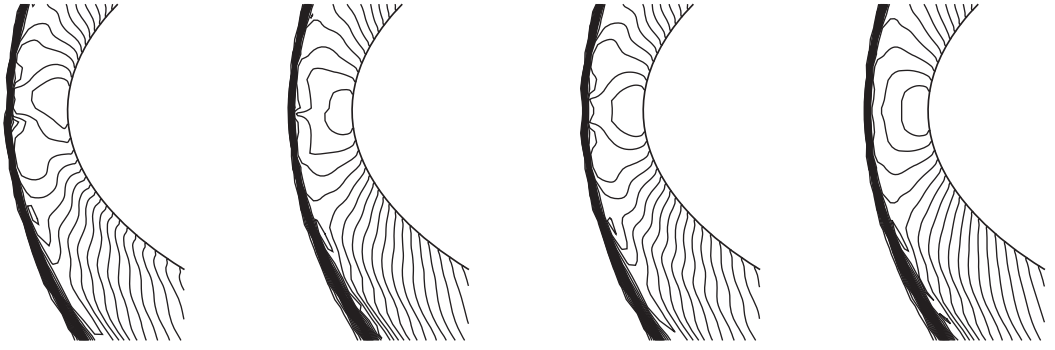

a) STVD $\zeta = 0.2$ b) Present $\zeta = 0.2$ c) STVD $\zeta = 0.3$ d) Present $\zeta = 0.3$

Fig. 6 Density contours for the blunt body case at Mach 8 and using a 128×66 mesh.

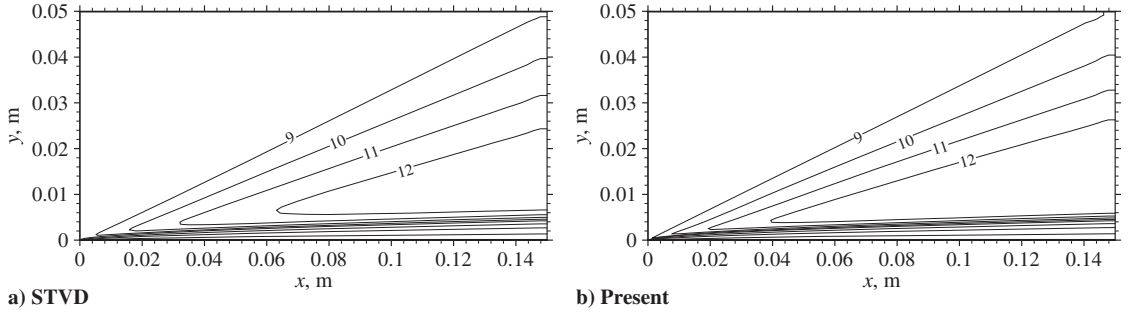

a) STVD b) Present

Fig. 7 Contours of x component of the Mach number for the hypersonic boundary-layer case using an 81^2 mesh.

and especially boundary layers at hypervelocities. Consider for instance a Mach 8.49 flow expanding 15.02 deg over a flat plate. Such effectively leads to the flow being accelerated to Mach numbers in excess of 12 before being slowed down at the lower surface through a boundary layer (see Fig. 7). For this problem, the inflow pressure and temperature are given values of 0.1 bar and 300 K, respectively. To capture the boundary layer efficiently, the grid is clustered at the wall such that the distance between the wall and the near-wall node is of 100 μm for a 41^2 mesh and, as the mesh is refined, decreased inversely proportional to the grid lines along the y coordinate.

The high Mach number of the flow entails substantial viscous dissipation effectively raising the temperature tenfold from the edge to the center of the boundary layer. Because the wall temperature is

Table 2 Surface heat flux for the hypersonic boundary-layer test case

		Heat flux to the surface at $x = 0.14$ m, kW/m^2			
Scheme	ζ	41^2 mesh	81^2 mesh	161^2 mesh	1281^2 mesh
MUSCL-TVD (minmod)	0.0	44.1	34.4	27.8	25.7
MUSCL-TVD (Van Leer)	0.0	17.0	19.3	21.6	25.2
STVD	0.0	27.5	26.4	25.7	25.2
Present	0.0	28.9	26.6	25.9	25.5
STVD	0.1	27.6	26.5	25.7	25.2
Present	0.1	28.9	26.6	25.9	25.5

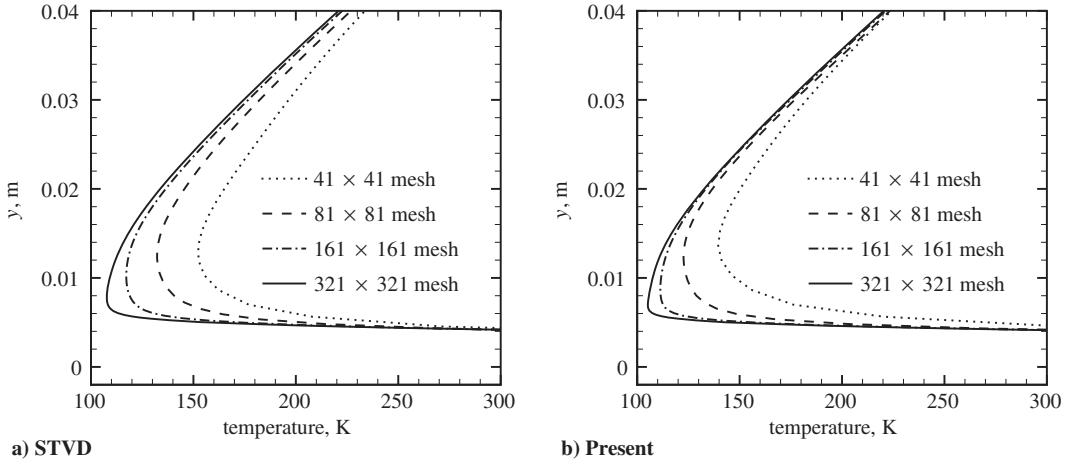

Fig. 8 Temperature profiles at $x = 0.14$ m for the hypersonic boundary-layer test case.

Downloaded by PUSAN NATL. UNIV. on January 17, 2017 | http://arc.aiaa.org | DOI: 10.2514/1.J055190

fixed to 300 K and is significantly less than the maximum temperature within the layer (~1000 K), a significant heat flux to the surface occurs. Such is particularly difficult to capture with high resolution because of its high sensitivity to the amount of dissipation introduced by the convective flux discretization scheme. For instance, as shown in Table 2, an accurate prediction of the heat flux at the wall can necessitate a mesh size almost 16 times greater when using the MUSCL reconstruction-evolution as opposed to the STVD scheme. Similarly to the STVD approach, the present method introduces minimal dissipation and offers an excellent approximation to the heat flux even on the coarsest mesh considered. Indeed, the proposed scheme achieves a similar level of accuracy using a 41^2 mesh than the MUSCL scheme does using a 161^2 mesh, thus yielding a more than 50-fold increase in computational efficiency. (This is due to the computing effort being proportional to the number of nodes

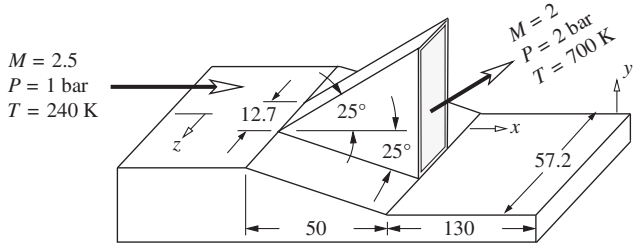

Fig. 9 Schematic of the ramp injector test case; all dimensions are in millimeters; surfaces of symmetry are imposed at $z = 0$ and $z = 28.6$ mm.

Table 3 Stagnation pressure difference for the ramp injector test case at $x = 0.085$ m[a]

		$\int_y \int_z \Delta P_\circ \, dz \, dy$, Pa · m^2	
Mesh	Nodes	STVD	Present
$90 \times 60 \times 30$	146,475	1060	1009
$135 \times 90 \times 45$	493,574	983	941
$203 \times 135 \times 68$	1,688,406	924	889
$304 \times 203 \times 101$	5,643,760	881	852

[a]The stagnation pressure difference $\Delta P_\circ$ corresponds to the difference between the freestream stagnation pressure and the local stagnation pressure determined from perfect gas relationships.

times the number of iterations, with the number of iterations typically increasing inversely proportional to the mesh spacing). Such a test case is also useful in verifying if our proposed eigenvalue conditioning does not introduce excessive dissipation within viscous layers. When ζ is set to 0.1 (the same value that is recommended to prevent carbuncles from occurring on bow shocks), almost no adverse effect can be observed on the resolution of the viscous layers either when using the multidimensional scheme or the dimensionally split approaches (see Table 2).

Not only is the proposed method advantaged resolution-wise over the MUSCL approach in capturing the heat flux at the wall, but it is also advantaged over the STVD in capturing the rarefaction wave. Indeed, as is apparent from the Mach number contours in Fig. 7 and the temperature profiles in Fig. 8, the present method yields in some

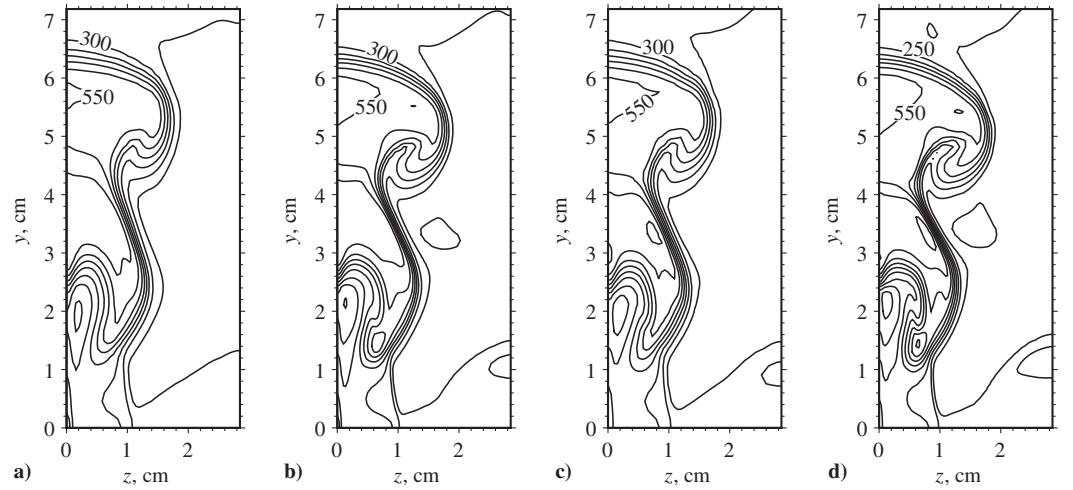

Fig. 10 Temperature profiles in kelvins at $x = 0.083$ m for the ramp injector test case: a) STVD, 0.5 million nodes; b) STVD, 1.7 million nodes; c) present scheme, 0.5 million nodes; and d) present scheme, 1.7 million nodes.

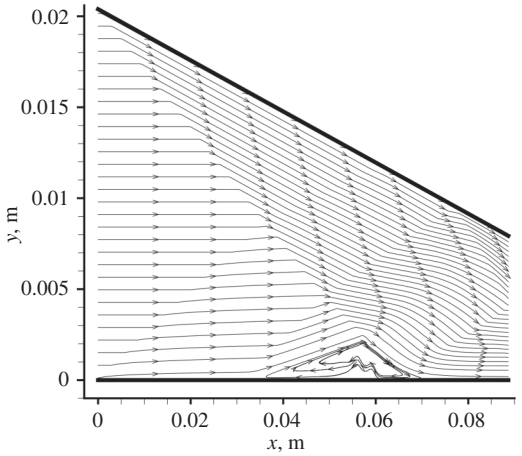

Fig. 11 Steady-state streamlines for the shock-induced separation test case using the present scheme and a 960^2 mesh.

regions a 1.5–2.0 increase in resolution per dimension compared to the STVD.

E. Ramp Injector

Another problem of interest to hypersonics is the so-called ramp injector (see Fig. 9), which is commonly used within scramjet airbreathing engines to mix fuel with the incoming air. The ramp injector achieves its high mixing efficiency through the generation of strong axial vortices, which originate from the bow shock generating a large pressure difference between the top of the injector and its sides. The axial vortices remain present within the flow for several injector lengths, effectively stretching the fuel–air surface area and hence increasing the mixing efficiency. In addition to being a problem of practical interest to airbreathing propulsion, it also is of interest in testing our method in resolving three-dimensional (3-D) axial vortices. For ease of reproducibility, we here prefer not to inject fuel but rather to inject air at different inflow conditions than the freestream as depicted in Fig. 9. Further, we here solve the Euler equations excluding viscous and heat transfer effects. Because there is no physical dissipation, the contact surface between the injectant and the incoming flow does not spread, no mixing occurs, and the axial vortices keep their strength over the entire domain.

In Fig. 10, a comparison of the temperature contours obtained on several meshes reveals that the proposed multidimensional scheme requires about one-third the number of nodes of the STVD to yield the same resolution of the axial vortices. This is confirmed through a comparison of the stagnation pressure difference on several meshes in Table 3; the dimensionally split approach requires the mesh to be refined by about three times to match the resolution of the genuinely multidimensional approach. Because the computing effort scales with the inverse of mesh spacing to the fourth power for a three-dimensional problem (should the number of iterations increase linearly with the number of grid lines per dimension), this translates into a four- to five-fold increase in computational efficiency when simulating 3-D axial vortices.

F. Shock-Induced Separation

The difficulty in simulating shock-induced separation regions at hypervelocities stems from the large variation of flow speeds involved, ranging from thousands of meters per second in the inviscid flow just above the bubble to a few tens of meters per second within the separated flow region. Thus, such a problem can provide a good test bed in determining the resolution capabilities of our numerical method not only in solving supersonic viscous boundary layers but also in solving low-subsonic viscous separated regions.

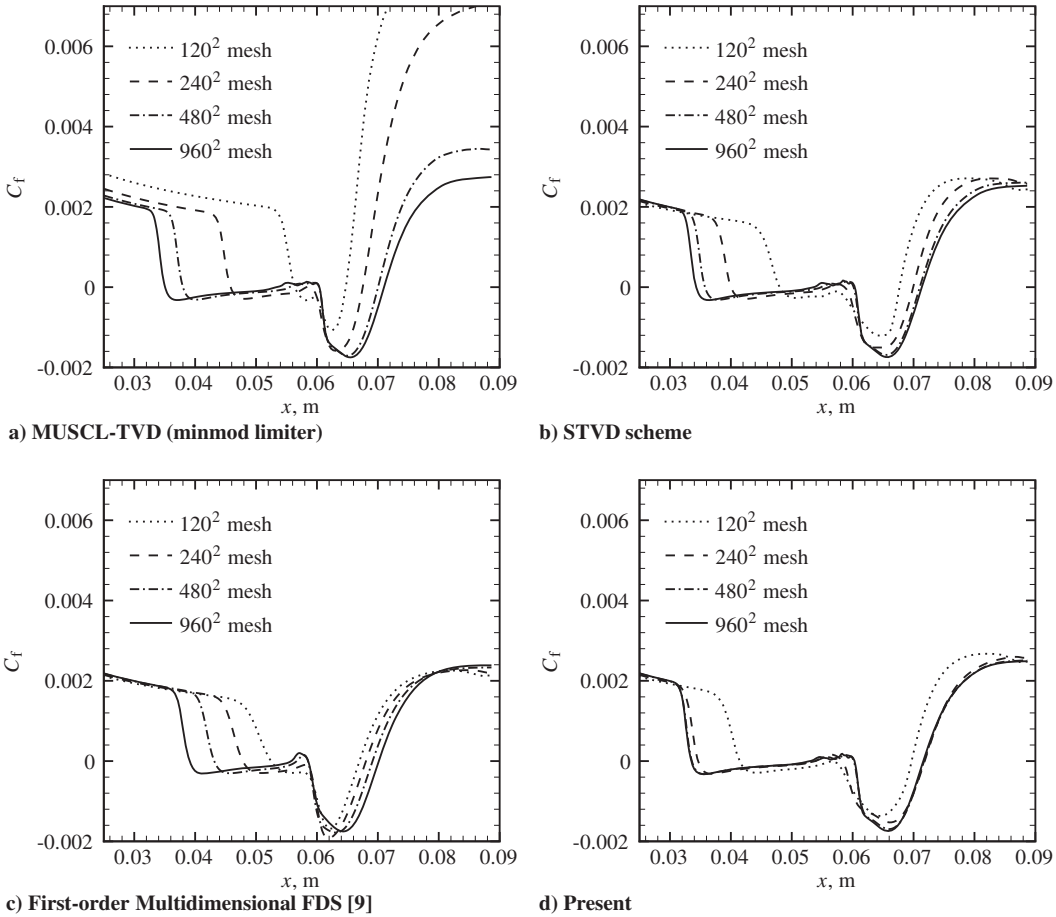

a) MUSCL-TVD (minmod limiter) **b) STVD scheme**

c) First-order Multidimensional FDS [9] **d) Present**

Fig. 12 Skin friction coefficient for the shock-induced separation test case.

Downloaded by PUSAN NATL. UNIV. on January 17, 2017 | http://arc.aiaa.org | DOI: 10.2514/1.J055190

Table 4 Effect of discretization scheme and grid size on the separation region length[a]

Scheme	Separation region length, cm			
	120^2 mesh	240^2 mesh	480^2 mesh	960^2 mesh
STVD	2.28	3.28	3.78	3.99
Present	3.14	4.04	4.14	4.15

[a]The separation region length is defined as the distance between the two x stations where $C_f = 0.0008$.

The shock–boundary-layer interaction problem here considered consists of air at Mach 4.8 with a pressure of 1 kPa and a temperature of 55.4 K entering a channel with the upper wall being inclined at an angle of 8 deg to generate a shock wave. Such a shock then impinges on the laminar boundary layer present on the lower wall, creates flow reversal, and reflects. The region of flow reversal is substantial and spans almost one-third of the computational domain, as can be observed from the streamtraces shown in Fig. 11. To resolve properly the boundary layer, the grid is constructed such that one-third of the grid lines along the y coordinate are equally spaced and located within a distance of 0.66 mm of the lower wall.

We here compare the present method to other Roe-based second-order schemes on the basis of skin friction coefficient to assess the capability of the schemes in capturing the size of the recirculation bubble as well as the shear stress at the wall. As is apparent from the skin friction profiles in Fig. 12, the present genuinely multidimensional method is considerably more accurate than other Roe-based schemes for this particular problem. The MUSCL reconstruction-evolution approach can again be seen to struggle in resolving compressible viscous layers; compared to the STVD scheme and the proposed multidimensional method, it requires a mesh approximately 16 times larger to yield the same error on the skin friction at the wall in the attached flow regions. Lowering the amount of artificial dissipation (by setting ζ to zero when conditioning the eigenvalues) did not solve this issue. Although using a more compressive Van Leer limiter did result in a significant improvement in resolution (especially with respect to the size of the separated region), the attached viscous layers remained tainted with significantly more artificial dissipation than when solved with a non-MUSCL scheme. (The results obtained with the Van Leer limiter are not shown here because a converged solution to steady state could not be obtained due to hangs early on in the convergence process, typically occurring after only one or two orders of magnitude of convergence.)

Contrary to the reconstruction-evolution strategies, the proposed method does not introduce excessive dissipation within the attached boundary layer and yields a skin friction coefficient in such regions that is as accurate as the one obtained with the STVD. Further, it is advantaged over the latter by yielding a significantly better resolution within the separated region, effectively leading to about a tenfold decrease in grid points for the same level accuracy (see comparison between the separation region length in Fig. 12 and in Table 4). This results in a more than 40-fold increase in computational efficiency for this particular problem because the number of iterations needed to reach convergence increases three to four times as the mesh spacing is halved.

VII. Conclusions

A new second-order accurate multidimensional flux difference splitting method is here presented. The scheme is such that it tends toward centered second-order accurate finite difference stencils in smooth flow regions but reverts to the first-order multidimensional flux difference splitting in the vicinity of shock waves or other discontinuities. Should the gradients in the second and third dimensions vanish, the proposed stencil collapses to the Yee symmetric total variation diminishing (STVD).

Various test cases of interest to supersonic and hypersonic flight reveal that the proposed method achieves typically a 1.5 to 2 times increase in resolution per dimension compared to the STVD approach. Such gains in resolution are problem-dependent, however, and tend to be more pronounced for flows where the waves propagate obliquely to the grid lines. Nonetheless, for some problems that are notoriously difficult to capture with compressible flow schemes (such as axial vortices generated by ramp injectors or boundary-layer separation due to shock impingement for instance), the present multidimensional approach is observed herein to yield a 5- to 40-fold increase in computational efficiency over its dimensionally split counterpart.

What makes such gains in resolution particularly noteworthy is that they are obtained while maintaining the desirable attributes of the STVD. That is, the proposed flux functions are in finite volume form, do not exhibit convergence hangs for a wide range of flows, yield solutions that are essentially monotonic, and can capture viscous layers with minimal dissipation. This is in contrast to other high-resolution stencils for high-speed flows (such as MUSCL-TVD or weighted essentially nonoscillatory), which achieve higher resolution of the convective waves at the expense of convergence hangs or of lower resolution of viscous layers.

The second-order multidimensional flux difference splitting proposed herein is hence particularly recommendable for simulating attached and separated viscous hypersonic flows because it yields a higher resolution of the skin friction or heat flux at the surfaces than competing strategies. In addition, its reliable convergence to machine accuracy over a wide range of conditions not only makes it suited to simulate steady-state problems but also ensures its compatibility with algorithms that depend on a reliable convergence of the residual.

References

[1] Roe, P. L., "Approximate Riemann Solvers, Parameter Vectors, and Difference Schemes," *Journal of Computational Physics*, Vol. 43, No. 2, 1981, pp. 357–372. doi:10.1016/0021-9991(81)90128-5

[2] Yee, H. C., Klopfer, G. H., and Montagné, J.-L., "High-Resolution Shock-Capturing Schemes for Inviscid and Viscous Hypersonic Flows," *Journal of Computational Physics*, Vol. 88, No. 1, 1990, pp. 31–61. doi:10.1016/0021-9991(90)90241-R

[3] Anderson, W. K., Thomas, J. L., and Van Leer, B., "Comparison of Finite Volume Flux Volume Flux Vector Splittings for the Euler Equations," *AIAA Journal*, Vol. 24, No. 9, 1986, pp. 1453–1460. doi:10.2514/3.9465

[4] Levy, D., Powell, K. G., and Van Leer, B., "Use of a Rotated Riemann Solver for the Two-Dimensional Euler Equations," *Journal of Computational Physics*, Vol. 106, No. 2, 1993, pp. 201–214. doi:10.1016/S0021-9991(83)71103-4

[5] Nishikawa, H., "Very Simple, Carbuncle-Free, Boundary-Layer-Resolving, Rotated-Hybrid Riemann Solvers," *Journal of Computational Physics*, Vol. 227, No. 4, 2008, pp. 2560–2581. doi:10.1016/j.jcp.2007.11.003

[6] Roe, P. L., "Discrete Models for the Numerical Analysis of Time-Dependent Multidimensional Gas-Dynamics," *Journal of Computational Physics*, Vol. 63, No. 2, 1986, pp. 458–476. doi:10.1016/0021-9991(86)90204-4

[7] Mena, J. G., Pepe, R., Lani, A., and Deconinck, H., "Assessment of Heat Flux Prediction Capabilities of Residual Distribution Method: Application to Atmospheric Entry Problems," *Communications in Computational Physics*, Vol. 17, No. 3, 2015, pp. 682–702. doi:10.4208/cicp.070414.211114a

[8] Huang, Y., and Lerat, A., "Second-Order Upwinding Through a Characteristic Time-Step Matrix for Compressible Flow Calculations," *Journal of Computational Physics*, Vol. 142, No. 2, 1998, pp. 445–472. doi:10.1006/jcph.1998.5935

[9] Parent, B., "Multidimensional Flux Difference Splitting Schemes," *AIAA Journal*, Vol. 53, No. 7, 2015, pp. 1936–1948. doi:10.2514/1.J053584

[10] Falcinelli, O. A., Elaskar, S. A., and Tamagno, J. P., "Reducing the Numerical Viscosity in Nonstructured Three-Dimensional Finite Volumes Computations," *Journal of Spacecraft and Rockets*, Vol. 45, No. 2, 2008, pp. 406–408. doi:10.2514/1.30688

[11] Venkatakrishnan, V., "Convergence to Steady State Solutions of the Euler Equations on Unstructured Grids with Limiters," *Journal of Computational Physics*, Vol. 118, No. 1, 1994, pp. 120–130. doi:10.1006/jcph.1995.1084

Downloaded by PUSAN NATL. UNIV. on January 17, 2017 | http://arc.aiaa.org | DOI: 10.2514/1.J055190

[12] Yee, H. C., "Construction of Explicit and Implicit Symmetric TVD Schemes and Their Applications," *Journal of Computational Physics*, Vol. 68, No. 1, 1987, pp. 151–179.
doi:10.1016/0021-9991(87)90049-0

[13] Bardina, J., and Lombard, C., "Three Dimensional Hypersonic Flow Simulations with the CSCM Implicit Upwind Navier–Stokes Method," *8th Computational Fluid Dynamics Conference*, AIAA Paper 1987-1114, 1987.

[14] MacCormack, R., "A New Implicit Algorithm for Fluid Flow," *13th Computational Fluid Dynamics Conference*, AIAA Paper 1987-2100, 1987.

[15] Parent, B., Shneider, M. N., and Macheret, S. O., "Detailed Modeling of Plasmas for Computational Aerodynamics," *AIAA Journal*, Vol. 54, No. 3, 2016, pp. 898–911.
doi:10.2514/1.J054624

[16] Gnoffo, P., and White, J. A., "Computational Aerothermodynamic Simulation Issues on Unstructured Grids," *37th AIAA Thermophysics Conference*, AIAA Paper 2004-2371, June–July 2004.

[17] Parent, B., "Positivity-Preserving High-Resolution Schemes for Systems of Conservation Laws," *Journal of Computational Physics*, Vol. 231, No. 1, 2012, pp. 173–189.
doi:10.1016/j.jcp.2011.09.006

[18] Parent, B., and Sislian, J., "The Use of Domain Decomposition in Accelerating the Convergence of Quasi-Hyperbolic Systems," *Journal of Computational Physics*, Vol. 179, No. 1, 2002, pp. 140–169.
doi:10.1006/jcph.2002.7048

C. Bailly
Associate Editor

Downloaded by PUSAN NATL. UNIV. on January 17, 2017 | http://arc.aiaa.org | DOI: 10.2514/1.J055190